Liquid-film coating on topographically patterned rotating cylinders

Weihua Li,[1] Marcio S. Carvalho,[2] and Satish Kumar[1,*]
[1]*Department of Chemical Engineering and Materials Science, University of Minnesota, Minneapolis, Minnesota 55455, USA*
[2]*Department of Mechanical Engineering, Pontificia Universidade Católica do Rio de Janeiro, Rio de Janeiro, Rio de Janeiro 22451-900, Brazil*
(Received 21 October 2016; published 21 February 2017)

The coating of discrete objects having surface topography is an important step in the manufacturing of a broad variety of products. To develop a fundamental understanding of this problem, we study liquid-film flow on rotating cylinders patterned with sinusoidal topographical features. The Stokes equations, augmented with a term accounting for centrifugal forces, are solved in a rotating reference frame using the Galerkin finite-element method (GFEM). A nonlinear evolution equation for the film thickness based on lubrication theory is also solved numerically and its predictions are compared to those from the GFEM calculations. When gravitational effects are negligible and the rotation rate is sufficiently low, liquid accumulates over the pattern troughs before merging to form multiple larger drops (located over troughs) whose number at steady state depends on the topography wavelength and rotation rate. When the rotation rate is sufficiently high, similar merging events occur, but liquid accumulates over the pattern crests at steady state. When gravitational forces become significant, it is possible to obtain a coating that closely conforms to the surface topography. The GFEM calculations are in agreement with predictions from the lubrication model provided the free-surface curvatures are sufficiently small. For sufficiently large pattern amplitude and film thickness, the GFEM calculations show that recirculation regions inside the troughs can appear and vanish as the cylinder rotates due to the variation of gravitational forces around the cylinder surface. This phenomenon, along with flow reversal over the crests, may strongly influence mixing, mass transport, and heat transport.

DOI: 10.1103/PhysRevFluids.2.024001

I. INTRODUCTION

The flow of liquid films on discrete objects is encountered in coating processes for products such as biomedical devices, automobiles, and food. Describing the shape of liquid films as they flow over discrete objects is a challenging task due to the complicated geometry of the object, the possible presence of object rotation, non-Newtonian rheology, and the occurrence of phenomena such as Marangoni flows and drying.

Flow of a thin liquid film on a cylinder that rotates about its horizontal axis is a common model problem for studying the coating of discrete objects and has attracted much attention since the pioneering work of Moffatt [1] and Pukhnachev [2]. When the cylinder rotation rate is below a critical value, gravity-driven drainage leads to a droplike liquid bulge that hangs from the underside of the cylinder and is supported by surface tension [3]. As the rotation rate is increased beyond the critical value, a steady smooth coating can be obtained with a thicker film on the upward-moving side and a thinner film on the downward-moving side [1]. In recent years, different flow regimes in this problem have been extensively investigated both theoretically and experimentally (see, e.g., [3–5]).

*Corresponding author: kumar030@umn.edu

 ©2017 American Physical Society

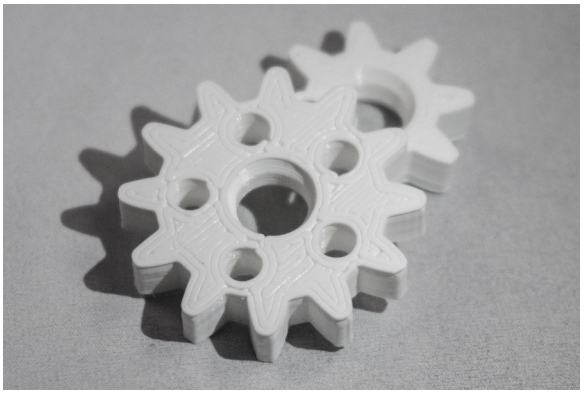

FIG. 1. Photograph of 3D printed gears, an example of topographically patterned cylinders.

The lubrication approximation has often been employed in previous studies to simplify the governing equations. Formally, this requires the film thickness to be much smaller than the cylinder radius and the slopes of the liquid-air interface to be small. To overcome these restrictions, Peterson *et al.* [6] used an adaptive finite-element scheme to solve the free-boundary problem involving the full Stokes equations. Their results reveal that the lubrication approximation works quite well even when the film thickness is a significant fraction ($\sim$40%) of the cylinder radius, especially under conditions where the ratio of the gravitational drainage rate to the cylinder rotation rate is not too large. When this ratio becomes too large, liquid shedding can occur and lead to interface shapes that are beyond the reach of lubrication theory.

Although most previous work assumes that the cylinder surface is perfectly smooth, in practice the cylinder surface may be uneven. This unevenness could be caused by surface imperfections or by imposed topographical patterns. The coating of substrates with topography occurs in the manufacturing of microelectronic devices [7], medical implants [8], and three-dimensional (3D) printed parts (Fig. 1) [9]. For planar substrates, the presence of topographical features can greatly modify film evolution and adversely influence the quality of the final coating [10]. Recirculation regions, for example, may form in topography valleys if both the topography waviness (the ratio of wave amplitude to wavelength) and film thickness are sufficiently large [11–14]. These recirculation regions may strongly influence mixing, mass transport, and heat transport and consequently the quality of the final (dried) coating [11,15–17].

The influence of topographical features on coating flows on rotating cylinders was first studied by Sahu and Kumar [18]. Applying the lubrication approximation, they derived and solved the governing equations for flow on a rotating cylinder patterned with sinusoidal topography. Their results reveal that when gravitational forces are negligible, steady states are reached where liquid tends to accumulate over the pattern troughs at low rotation rates and over the pattern crests at high rotation rates. When gravitational forces are significant, steady states cannot be attained, in contrast to the case of an unpatterned cylinder. The present paper extends the work of Ref. [18] to study the more general case where the lubrication approximation is removed.

To do this, we employ the Galerkin finite-element method (GFEM) and also compare our results to those obtained from a lubrication model. Both modeling approaches are described in Sec. II. Coating flows on rotating cylinders patterned with sinusoidal topography are studied in Secs. III and IV, where gravitational effects are absent and present, respectively. Conclusions are given in Sec. V.

II. MATHEMATICAL MODEL

We consider flow of a Newtonian liquid with constant viscosity μ, density ρ, and surface tension σ on a topographically patterned rotating cylinder. For a cylinder with mean radius R_{mean}, its surface

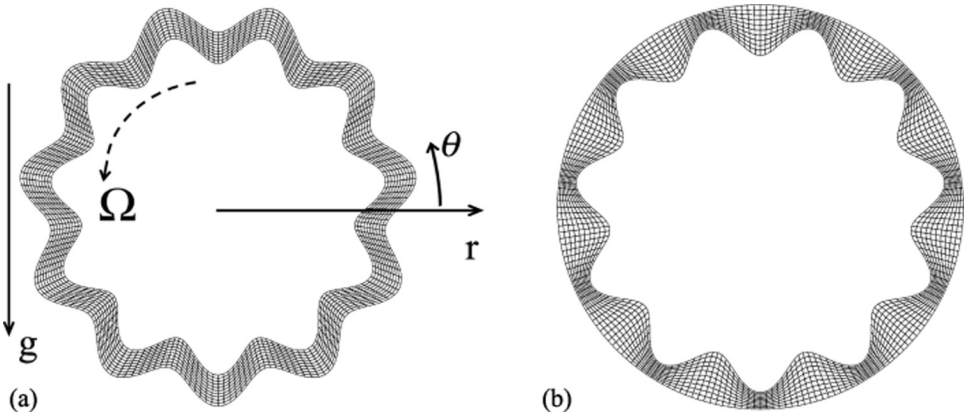

FIG. 2. Problem geometry and sample finite-element meshes for two different initial conditions: (a) IC 1, uniform thickness, and (b) IC 2, constant radius.

$R(\theta)$ can be expressed as

$$R = R_{\text{mean}} + \mathcal{B}(\theta), \tag{1}$$

where $\mathcal{B}(\theta)$ describes the shape of the topography as a function of the angular coordinate. For a sinusoidal surface topography (Fig. 2), $\mathcal{B}(\theta) = \delta \sin(\omega\theta)$, where δ and ω are the topography amplitude and (integer) frequency, respectively. The cylinder is rotating about its horizontal axis at constant angular speed Ω in the counterclockwise direction. We are interested in the evolution of the film thickness around the cylinder circumference, so any axial variations are neglected.

A. Governing equations

For studying liquid flow on a rotating cylinder, it is convenient to solve the governing equations in a rotating frame of reference. We employ polar coordinates with unit vectors $\mathbf{e}_r$, $\mathbf{e}_\theta$, and $\mathbf{e}_z$. The corresponding momentum balance equations can be written as [19]

$$\rho[\mathbf{u}_t + \mathbf{u}\cdot\nabla\mathbf{u}] = -\nabla p + \mu\nabla^2\mathbf{u} - \rho\boldsymbol{\Omega}\times(\boldsymbol{\Omega}\times\mathbf{r}) - 2\rho\boldsymbol{\Omega}\times\mathbf{u} + \rho\mathbf{g}, \tag{2}$$

where p is pressure, $\mathbf{u} = w\mathbf{e}_r + u\mathbf{e}_\theta$ is the velocity vector, t is time, $\mathbf{g} = g\mathbf{e}_g = -g\sin(\theta+\Omega t)\mathbf{e}_r + [-g\cos(\theta+\Omega t)]\mathbf{e}_\theta$ is the gravitational field, $\boldsymbol{\Omega} = \Omega\mathbf{e}_z$ is the angular velocity, and $\mathbf{r}$ is the position vector of a fluid element.

Following Refs. [3,18], we scale length with R_{mean}, velocity with $U = \rho g R_{\text{mean}}^2/\mu$, time with R_{mean}/U, and pressure with $\mu U/R_{\text{mean}}$. The scaled governing equations are

$$\nabla\cdot\mathbf{u} = 0, \tag{3}$$

$$\text{Re}[\mathbf{u}_t + \mathbf{u}\cdot\nabla\mathbf{u}] = -\nabla p + \nabla^2\mathbf{u} - W^2\mathbf{r} - 2\,\text{Re}_\Omega(\mathbf{e}_z\times\mathbf{u}) + \mathbf{e}_g, \tag{4}$$

where

$$W = \frac{\Omega}{\sqrt{g/R_{\text{mean}}}}, \quad \text{Re} = \frac{\rho^2 g R_{\text{mean}}^3}{\mu^2}, \quad \text{Re}_\Omega = \frac{\rho\Omega R_{\text{mean}}^2}{\mu}.$$

Here W is the dimensionless rotation rate, Re is a Reynolds number based on a gravitational drainage velocity ($\rho g R_{\text{mean}}^2/\mu$), and Re_Ω is a Reynolds number based on the cylinder velocity ($R_{\text{mean}}\Omega$).

To simplify the governing equations, we neglect inertial effects arising from gravitational drainage ($\text{Re}[\mathbf{u}_t + \mathbf{u}\cdot\nabla\mathbf{u}]$) and cylinder rotation [$2\,\text{Re}_\Omega(\mathbf{e}_z\times\mathbf{u})$]. However, following Refs. [3,20], we still

TABLE I. Order-of-magnitude estimates of dimensional quantities. The viscosity, density, and surface tension are representative of a glycerol-water mixture.

Constants	Typical values
mean cylinder radius R_{mean} (cm)	1
rotation rate Ω (rad/s)	10^{-1}–10^{1}
viscosity μ (cP)	300
density ρ (g/cm^3)	1
surface tension σ (dyn/cm)	10^{1}–10^{2}
characteristic film thickness H (cm)	10^{-3}–0.1

retain the centrifugal term ($W^2\mathbf{r}$). With these changes, Eq. (4) becomes

$$\mathbf{0} = -\nabla p + \nabla^2\mathbf{u} - W^2\mathbf{r} + \mathbf{e}_g. \tag{5}$$

At the cylinder surface $r = R(\theta) = R_{\text{mean}} + \delta\sin(\omega\theta)$, we apply no-slip and no-penetration conditions

$$\mathbf{t}\cdot\mathbf{u} = 0, \quad \mathbf{n}\cdot\mathbf{u} = 0, \tag{6}$$

where $\mathbf{n}$ and $\mathbf{t}$ are the unit outward normal and tangent vectors.

At the free surface, the liquid needs to satisfy the kinematic and interfacial-stress boundary conditions

$$\mathbf{n}\cdot\mathbf{u} = \mathbf{n}\cdot\dot{\mathbf{r}}, \tag{7}$$

$$\mathbf{n}\cdot\mathbf{T} = -\frac{\kappa}{\text{Bo}}\mathbf{n}, \tag{8}$$

where $\mathbf{T}$ is the total stress tensor, the components of which are nondimensionalized by $\mu U/R_{\text{mean}}$. The Bond number $\text{Bo} = \rho g R_{\text{mean}}^2/\sigma$ is a measure of the importance of surface-tension forces relative to gravitational forces and $\kappa = \nabla\cdot\mathbf{n}$ is the surface curvature. The dot above the $\mathbf{r}$ in Eq. (7) denotes a temporal derivative.

Order-of-magnitude estimates for key dimensional quantities are listed in Table I. For the applications that motivate this work, the characteristic film thickness H is at least an order of magnitude smaller than the mean cylinder radius R_{mean}, so lubrication theory can be used to estimate the strength of inertial forces. Using lubrication scalings, the Reynolds number becomes $\text{Re} = \rho g H^2 R_{\text{mean}}/\mu^2$, while Re_Ω has the same definition as before, and both of these are multiplied by ϵ^2 in the governing equations, where $\epsilon = H/R_{\text{mean}}$ [3]. For the parameter values listed in Table I, $\epsilon^2\text{Re}$ and $\epsilon^2\text{Re}_\Omega$ are both no more than $O(10^{-1})$, justifying our neglect of these inertial terms. Inertial effects may become important for thicker films, less viscous liquids, and faster rotation rates and lead to an even richer range of behavior than that reported here.

The equations associated with the above 2D model are solved numerically with the GFEM. The GFEM results are used to assess the validity of a lubrication-theory-based model (Sec. II C). The 2D model allows us to keep all nonlinearities of the system and thus study with confidence flow regimes where the lubrication model is not formally valid. However, due to the high computational costs associated with the 2D model, for some of the calculations conducted in the thin-film regime in Secs. III and IV, only results from the lubrication model are presented.

B. The 2D finite-element method

The Galerkin finite-element method with continuous biquadratic basis functions for velocity and position, and discontinuous linear basis functions for pressure, is used to solve Eqs. (3) and (5) subject to boundary conditions (6) and (8). The unknown flow domain (x, y) is mapped onto a

reference computational domain (ξ,η) by elliptic mesh generation [21]. The free surface of the liquid is located by applying the kinematic condition (7). At a given instant in time, we solve the following set of elliptic partial differential equations simultaneously with the other governing equations in the computational domain:

$$\nabla\cdot(D_\xi\nabla\xi)=0,\quad \nabla\cdot(D_\eta\nabla\eta)=0, \tag{9}$$

where D_ξ and D_η are mesh diffusion coefficients used to distribute elements within the physical domain.

A second-order adaptive time-stepping algorithm is used for time integration. In the first three fixed time steps, a first-order Euler forward-difference predictor and a first-order Euler backward-difference corrector are used to alleviate spurious oscillations in the solution; this improves the convergence rate in subsequent simulations [22]. A second-order Adams-Bashforth predictor is used with the trapezoid rule as a corrector in the following time steps to evaluate the local time truncation errors and to adjust the next time-step size. The nonlinear system of algebraic equations obtained by application of the trapezoid rule to the weak forms of Eqs. (3), (5), and (9) is solved by the Newton-Raphson method and the iterative process is finished when the norm of the difference between two consecutive residuals is smaller than 10^{-5}.

We perform simulations with two different initial conditions (ICs) for the liquid film that coats the cylinder: IC 1, uniform thickness [Fig. 2(a)], and IC 2, constant radius [Fig. 2(b)]. For our calculations, 2000 elements (200 elements in the axial direction and 10 elements in the radial direction) were found to be sufficient. Conservation of total mass is monitored and the results are considered accurate when $100(V_{\max}-V_{\min})/V_{\text{ini}}<0.1\%$, where $V_{\max}$ and $V_{\min}$ are the maximum and minimum volumes of the liquid during the entire calculation, respectively, and V_{ini} is the initial volume [23].

C. Lubrication theory

Following Ref. [18], lubrication theory can be applied to derive a nonlinear evolution equation for the film thickness h,

$$\frac{\partial h}{\partial t}=\frac{\partial}{\partial\theta}\left[\frac{h^3}{3}\cos(\theta+MWt)-\frac{h^3}{3\,\text{Bo}}\left(\frac{\partial h}{\partial\theta}+\frac{\partial^3 h}{\partial\theta^3}\right)-\frac{h^3}{3}[W^2-\sin(\theta+MWt)]\frac{\partial h}{\partial\theta}\right]$$
$$-\frac{\partial}{\partial\theta}\left(\frac{h^3}{3\,\text{Bo}}[\delta\omega\cos(\omega\theta)-\delta\omega^3\cos(\omega\theta)]+\frac{h^3}{3}[W^2-\sin(\theta+MWt)]\delta\omega\cos(\omega\theta)\right), \tag{10}$$

where $M=\mu/\rho\sqrt{gR_{\text{mean}}}$ is the dimensionless viscosity. In deriving this equation, we have assumed that $\epsilon=H/R_{\text{mean}}\ll 1$ and we have rescaled all lengths by R_{mean} to be consistent with the equations of Sec. II A.

This evolution equation allows for the study of nonlinear phenomena at a relatively modest cost compared to solving the full governing equations with the GFEM. We note that Eq. (10) is a corrected version of Eq. (43) in Ref. [18]; an extra factor of 2 in front of $\delta\omega\cos(\omega\theta)$ in the last term appeared in the latter equation (see [24]). For a cylinder patterned with sinusoidal topography, the lubrication approximation is expected to work well when the pattern wavelength is much greater than the characteristic film thickness H ($\omega H\ll R_{\text{mean}}$) and the topography amplitude is much less than the cylinder radius $\delta\ll 1$ [18].

For a fixed set of problem parameters (δ, ω, Bo, M, and W), we solve Eq. (10) numerically by applying a partially implicit finite-difference scheme [3,25]. Film thickness is obtained over 400 uniformly discretized nodes at a given instant of time in a reference frame rotating with the cylinder. Solution accuracy is checked in a manner similar to that described in Sec. II B.

III. RESULTS FOR THE ZERO-GRAVITY CASE

We first study the case of a cylinder with sinusoidal topography that is spinning so rapidly that gravitational effects are negligible. It is no longer appropriate to take the drainage rate as the characteristic velocity in this regime, so we rescale the governing equations by using σ/μ and σ/R_{mean} as the new characteristic velocity and pressure (stress), respectively. When all gravitational terms are neglected, Eqs. (5) and (10) become

$$0 = -\nabla p + \nabla^2 \mathbf{u} - S\mathbf{r}, \tag{11}$$

$$\frac{\partial h}{\partial t} = -\frac{1}{3}\frac{\partial}{\partial \theta}\left[h^3\left(\frac{\partial h}{\partial \theta} + \frac{\partial^3 h}{\partial \theta^3} + S\frac{\partial h}{\partial \theta} + \delta\omega\cos(\omega\theta) - \delta\omega^3\cos(\omega\theta) + S\delta\omega\cos(\omega\theta)\right)\right], \tag{12}$$

where $S = \rho\Omega^2 R_{\text{mean}}^3/\sigma$ can be interpreted as an inverse Weber number or dimensionless rotation rate.

For an unpatterned cylinder ($\delta = 0$), the evolution equation (12) reduces to that studied in Ref. [3]. Linear stability analysis reveals that perturbations with wave number $k < k_{\text{cutoff}}$ grow in amplitude under the action of centrifugal forces, while those with $k > k_{\text{cutoff}}$ are leveled by surface tension. The cutoff wave number k_{cutoff} is

$$k_{\text{cutoff}} = [\sqrt{1+S}], \tag{13}$$

where $[x]$ is the greatest integer less than x. This instability growth rate $\hat{\omega}$ is

$$\hat{\omega} = \tfrac{1}{3}\{(1+S)k^2 - k^4\}h_0^3, \tag{14}$$

where h_0 is the dimensionless mean film thickness.

The fastest-growing wave number k_{max} has the form

$$k_{\text{max}} = \sqrt{(1+S)/2}. \tag{15}$$

Numerical solutions of Eq. (12) show that unstable disturbances grow to form a steady state in which drops on the cylinder surface are separated by thin films [3]. Thus, k_{max} indicates the number of drops expected on an unpatterned cylinder at steady state. We note that here and elsewhere in the paper, the steady states we report reflect the long-time behavior of the coating. Thus, they should be regarded as apparent steady states since we do not solve for the steady states directly.

To validate our numerical solutions, we extracted growth rates of perturbations having different wave numbers on an unpatterned cylinder using a representative mean film thickness of $h_0 = h(\theta, t = 0) = 0.1$. Results from the 2D model and lubrication model are in good agreement at low k (Fig. 3) over a broad range of rotation rates S. However, with increasing k, which corresponds to higher curvature at the free surface, the agreement worsens and the lubrication model overestimates the leveling rate (smaller growth rate). Since faster leveling is related to stronger capillary flows, the lubrication model tends to overestimate the effects of surface tension in regions where the free-surface curvature is large. Although not shown here for brevity, the growth rates extracted from numerical solution of Eq. (12) agree well with the linear stability result (14) for all k.

For a topographically patterned cylinder ($\delta \neq 0$), it was observed in Ref. [18] that liquid tends to accumulate over the pattern troughs at low rotation rates and over the pattern crests at high rotation rates. Although this transition occurs over a range of rotation rates, it would be useful to have a single value that characterizes the transition. We refer to this value as the critical rotation rate S_{critical} and have found that it can be estimated from Eq. (13). Suppose that the cylinder pattern creates a perturbation at the free surface with $k = \omega$, as would happen if one had an initial condition of uniform film thickness (Fig. 2). Then, inversion of Eq. (13) yields

$$S_{\text{critical}} = \omega^2 - 1. \tag{16}$$

For $S < S_{\text{critical}}$, a film having an initially uniform thickness would be expected to level at short times, driving liquid into the pattern troughs. Because there is more liquid in the troughs, centrifugal

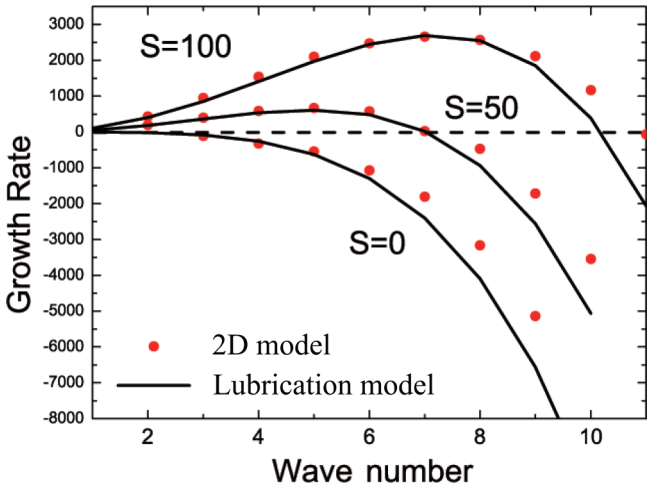

FIG. 3. Growth rates versus wave number in the absence of gravity on an unpatterned cylinder with $h_0 = 0.1$.

forces would be stronger there and the liquid would be expected to thicken there at longer times. For $S > S_{\text{critical}}$, centrifugal forces would overwhelm the short-time leveling and drops would be expected to form over the crests, where the centrifugal forces are stronger due to their greater distance from the cylinder center. Note that S_{critical} increases as the pattern frequency does, reflecting the fact that shorter-wavelength disturbances are leveled (by surface tension) more easily.

In the following sections, we explore the nonlinear behavior of the film in the zero-gravity regime using numerical solutions of the lubrication model (12) and the 2D model (11). Following Ref. [18], we initially fix the pattern amplitude at $\delta = 0.01$ and the mean film thickness at $h_0 = 0.02$ and examine the cases where $S < S_{\text{critical}}$ (Sec. III A) and $S > S_{\text{critical}}$ (Sec. III B). We then consider the case of larger pattern amplitude (Sec. III C).

A. The case $S < S_{\text{critical}}$

We first consider a cylinder with pattern frequency $\omega = 11$, where the corresponding critical rotation rate is $S_{\text{critical}} = 120$. To characterize film evolution, in Fig. 4 we plot the maximum film

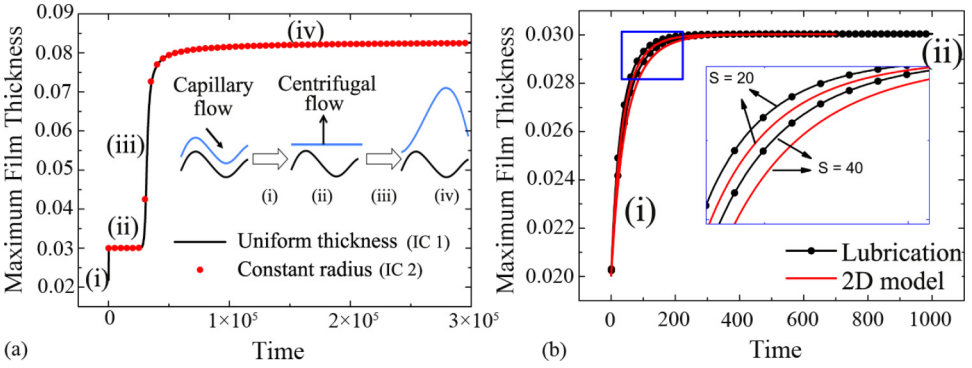

FIG. 4. Time variation of maximum film thickness on a patterned cylinder with $\delta = 0.01$, $\omega = 11$, $h_0 = 0.02$, and $S_{\text{critical}} = 120$. (a) Results obtained with the lubrication model for $S = 40$ and two different initial conditions. (b) Results obtained with the lubrication model and the 2D model in stages (i) and (ii) for different values of S with an initial film of uniform thickness.

thickness as a function of time in the regime where $S < S_{\text{critical}}$. Two different initial conditions are considered: (i) a film of uniform thickness and (ii) a film of constant radius (Fig. 2).

Figure 4(a) shows that the steady maximum film thickness predicted by the lubrication model is independent of the initial condition. In addition, if the initial film is of uniform thickness, the formation of drops follows four distinct stages, which we summarize here using $S = 40$ as a representative case. In stage (i), capillary forces are stronger than centrifugal forces, driving liquid from the pattern crests to the pattern troughs, which leads to a coating of constant radius in stage (ii). Since the coating is thicker over the troughs and thinner over the crests, the centrifugal forces on the liquid over the troughs are stronger and thus produce liquid drops over the troughs in stage (iii). These drops rapidly grow in size until the coating reaches a steady state in stage (iv), where centrifugal forces are balanced by surface-tension forces. If the initial film is of uniform radius, then the film starts in stage (ii) and goes through stages (iii) and (iv).

In Fig. 4(b) we focus on stages (i) and (ii), plotting the evolution of the maximum film thickness for $S = 20$ and 40. The maximum film thickness in stage (ii) is independent of S; however, an increase in S hinders the rate of leveling (smaller maximum film thickness) in stage (i). This is simply because a higher value of S leads to stronger centrifugal forces on the liquid over the crests, which slows down the capillary leveling. The comparison in Fig. 4(b) between results obtained from the lubrication model and the 2D model suggests that the lubrication model tends to overpredict the leveling rate, which is consistent with our earlier observation that the effects of surface tension are overestimated by the lubrication model.

To investigate the influence of rotation rate on liquid motion, in Fig. 5 we plot the steady film-thickness profiles and free-surface profiles [stage (iv)] calculated with the lubrication model. These steady states occur at late times ($t \sim 10^5$) [Fig. 4(a)]. Simulations with such extensive durations are computationally prohibitive with our GFEM scheme due to the small time-step size needed in the zero-gravity regime. Thus, only results from the lubrication model are shown in Fig. 5.

For a relatively small rotation rate $S = 10$ [Figs. 5(a) and 5(b)], liquid accumulating in adjacent troughs partially merges to form larger drops that span several troughs. As the value of S (and thus the centrifugal force) is increased [Figs. 5(c) and 5(d)], several drops of nearly uniform size and spacing form and these are located over troughs. However, further increasing the rotation rate breaks the uniformity of drop size and causes an uneven distribution of liquid on the cylinder surface, as can be seen in Figs. 5(e) and 5(f). The behavior shown in Fig. 5 clearly indicates that the steady film profile on a patterned cylinder is highly sensitive to the rotation rate in the regime where $S < S_{\text{critical}}$.

Note that for unpatterned cylinders with $S = 10$, 40, and 100, the fastest growing wave number $k_{\max}$ [calculated from Eq. (15)] is two, four, and seven, respectively. This indicates that two drops will develop on the cylinder when $S = 10$, six drops will develop when $S = 40$, and ten drops will develop when $S = 100$ at steady state when surface topography is absent [3,18]. However, Figs. 5(d) and 5(f) show that with the presence of surface topography, the number of drops is five for $S = 40$ and four for $S = 100$. These do not match the corresponding values of $k_{\max}$, indicating that even small-amplitude surface topography significantly modifies the liquid distribution around the cylinder when $S < S_{\text{critical}}$. As the mismatch worsens as S increases, the influence of surface topography becomes more pronounced as the rotation rate (centrifugal force) increases. Moreover, for a fixed value of S, a decrease in ω leads to fewer troughs on the cylinder and therefore fewer drops, as shown in Fig. 6.

Finally, we briefly comment about the possible influence of several other parameters for which we have not been able to perform exhaustive studies. As film thickness increases for fixed topography amplitude, we expect that the influence of topography will be diminished due to increasing disparity in the two length scales. Based on the results of Ref. [18], we expect that as the rotation rate increases, the topography amplitude required to trigger the effects we have observed will decrease due to the stronger centrifugal forces. As the pattern frequency decreases, the topography amplitude required to trigger the effects we have observed is expected to decrease as well due to lower free-surface curvatures (and thus slower film leveling).

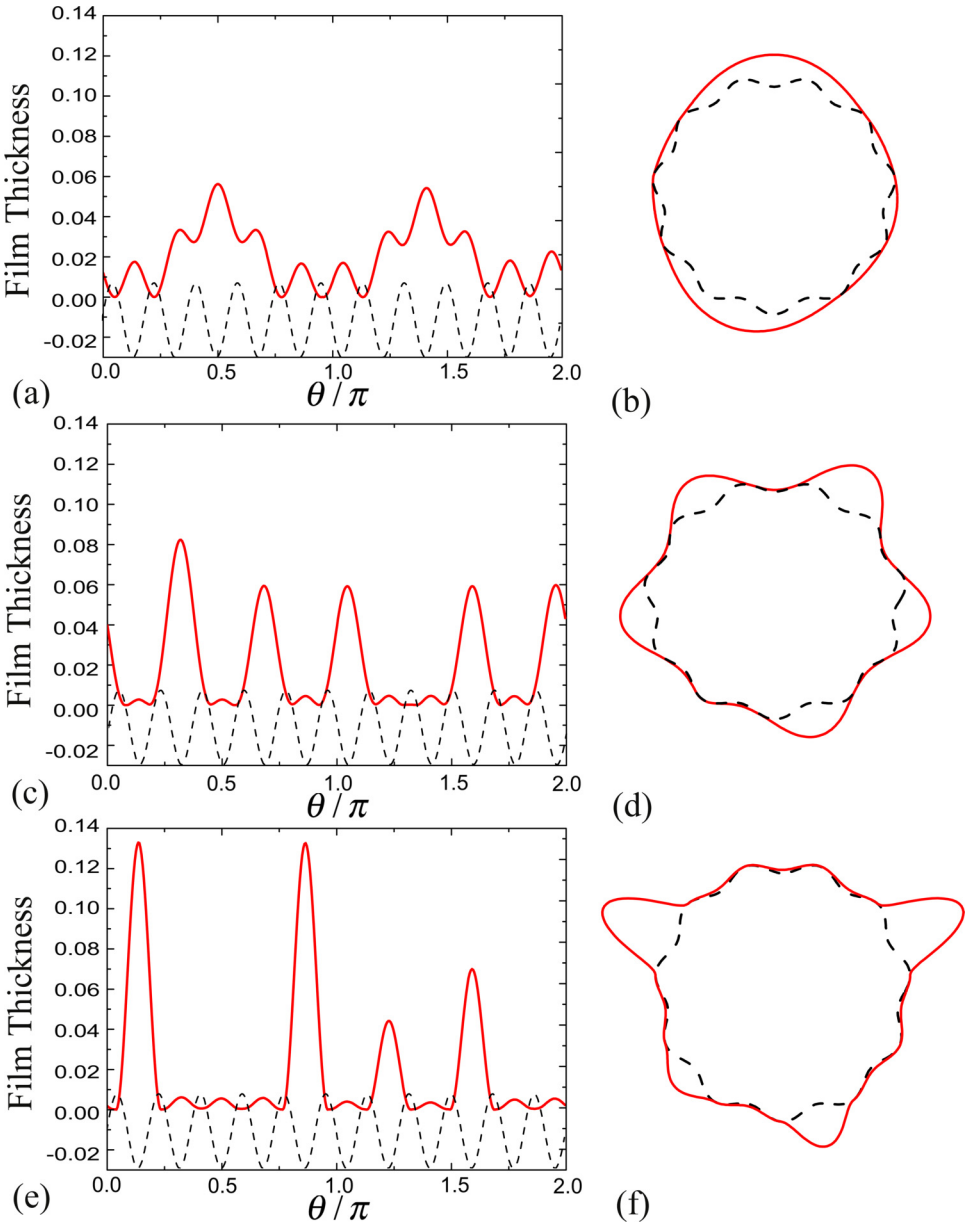

FIG. 5. Steady film-thickness profiles and corresponding free-surface profiles obtained from the lubrication model with $\delta = 0.01$, $\omega = 11$, and $h_0 = 0.02$ for (a) and (b) $S = 10$, (c) and (d) $S = 40$, and (e) and (f) $S = 100$. Initial conditions are films of uniform thickness. Dashed lines indicate surface topography. For ease of visualization, in (b), (d), and (f), the film thickness and pattern amplitude plotted are five times larger than the actual values.

B. The case $S > S_{\text{critical}}$

We now turn to the regime where $S > S_{\text{critical}}$ and consider the case $S = 160$ as a representative example. In Fig. 7(a) we plot the time variation of the maximum film thickness obtained with the lubrication model starting from initial films of constant radius and uniform thickness. The results

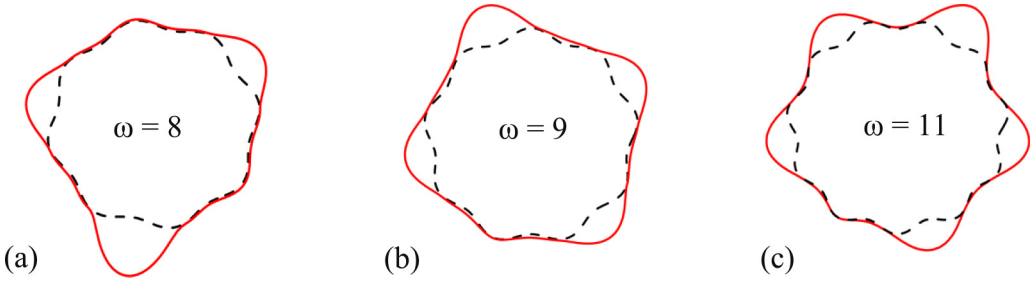

FIG. 6. Steady free-surface profiles obtained from the lubrication model with $\delta = 0.01$, $S = 40$, and $h_0 = 0.02$ for (a) $\omega = 8$, (b) $\omega = 9$, and (c) $\omega = 11$. Initial conditions are films of uniform thickness. Dashed lines indicate surface topography. For ease of visualization, the film thickness and pattern amplitude plotted are five times larger than the actual values.

suggest that the steady film-thickness profile strongly depends on the initial film condition, in contrast to the case where $S < S_{\text{critical}}$. For an initial coating of uniform thickness (black solid line), higher centrifugal forces on the liquid over the crests lead to the flow of liquid from surrounding areas and the formation of drops over the crests. The coating reaches a steady state almost immediately with drops of almost the same size connected by very thin films over the troughs. Here the number of drops is equal to the pattern frequency. The corresponding steady film-thickness profile and free-surface profile are plotted in Figs. 8(a) and 8(b).

A similar time history of film evolution is also observed with the 2D model, shown in Fig. 7(b) with a black solid line. Note that the time period shown in Fig. 7(b) is much shorter than that in Fig. 4(a), reflecting faster growth of free-surface perturbations at higher S. As can be seen in Fig. 8(a), the film-thickness profile predicted by the 2D model agrees well with the prediction from the lubrication model. The maximum film thickness predicted by the lubrication model is slightly smaller, which can be understood by recalling that this model tends to overestimate the effects of surface tension.

For an initial coating of constant radius [red solid line in Fig. 7(a)], the lubrication model predicts that film evolution follows four stages when $S > S_{\text{critical}}$. In stages (i) and (ii), centrifugal forces are stronger on the liquid over the troughs (relative to the liquid on the crests), producing drops over the troughs (similar to what is observed when $S < S_{\text{critical}}$). The film-thickness profile and free-surface profile are shown in Figs. 8(c) and 8(d). However, these drops are not stable when

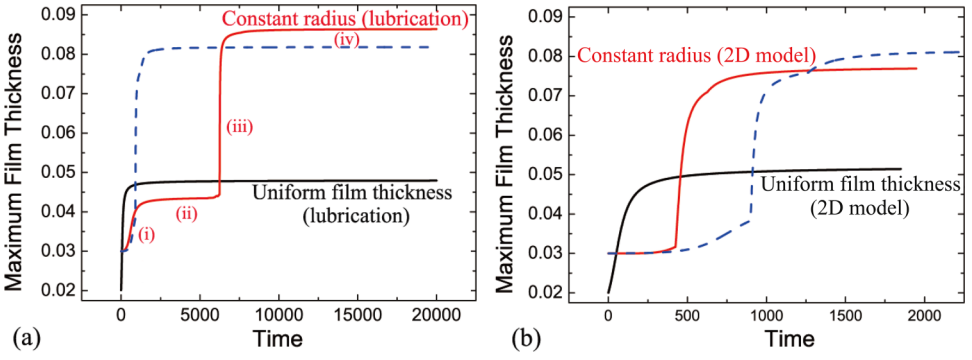

FIG. 7. Time variation of the maximum film thickness with $S = 160$ ($> S_{\text{critical}}$), $\delta = 0.01$, $\omega = 11$, and $h_0 = 0.02$. Results are obtained with the (a) lubrication model and (b) 2D model. Results obtained by using the lubrication model with an initial film of constant radius and a superimposed perturbation are plotted in both panels for comparison (blue dashed line).

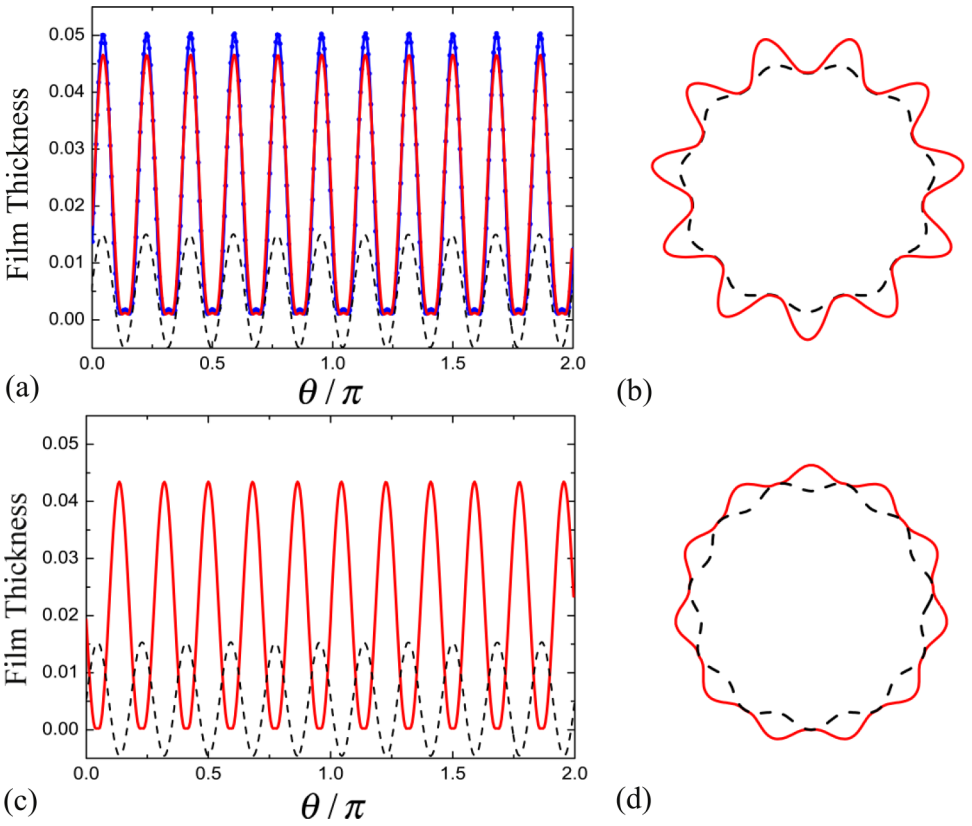

FIG. 8. (a) and (c) Film-thickness profiles and (b) and (d) free-surface profiles obtained with the lubrication model (red solid line) and the 2D model (blue dotted line) at $t = 2000$ with $S = 160$, $\delta = 0.01$, $\omega = 11$, and $h_0 = 0.02$. Initial conditions are films of (a) and (b) uniform thickness and (c) and (d) constant radius [results from the 2D model are only shown in (a)]. Dashed lines indicate surface topography. For ease of visualization, in (b) and (d) the film thickness and pattern amplitude plotted are five times larger than the actual values.

located over the troughs and tend to shift to the crests in stage (iii). During this shifting process liquid is redistributed, leading to uneven drop sizes.

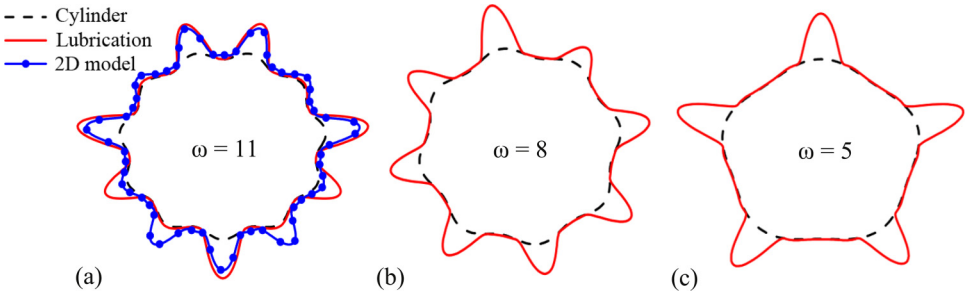

FIG. 9. Steady free-surface profiles with $S = 160$, $\delta = 0.01$, and $h_0 = 0.02$ for (a) $\omega = 11$, (b) $\omega = 8$, and (c) $\omega = 5$. Initial conditions are films of constant radius and no noise added. For ease of visualization, the film thickness and pattern amplitude plotted are five times larger than the actual values.

The coating reaches a steady state in stage (iv) and we plot in Fig. 9(a) the corresponding free-surface profile. The liquid is unevenly distributed on the cylinder, with seven main drops and four smaller drops over the crests, in contrast to the case where the initial condition is a film of uniform thickness [Fig. 8(b)]. Note that the total number of drops is equal to the pattern frequency ($\omega = 11$).

The time variation of the maximum film thickness predicted by the 2D model for an initial coating of constant radius is shown in Fig. 7(b) (red solid line). There are marked differences from the result predicted by the lubrication model [red solid line in Fig. 7(a)]. Both the 2D model and the lubrication model predict that drops form over the troughs initially, but the 2D model predicts that liquid redistribution and a steady state occur much earlier. As can be seen in Fig. 9(a), the number of main drops and their sizes, but not their location, are in good agreement with those predicted by the lubrication model.

Although not shown here, both models predict that as the value of S increases, the size of the main drops tends to increase (due to the stronger centrifugal forces). Although the locations of the drops change, the total number of drops (which is equal to the pattern frequency) does not. (The drops also grow more quickly as S increases.) Thus, when $S > S_{\text{critical}}$, the film profile on a patterned cylinder does not appear to be as sensitive to the rotation rate as it does when $S < S_{\text{critical}}$.

To explain the discrepancy between the lubrication and 2D predictions for the constant-radius initial condition, we perform simulations using the lubrication model with an initial coating of constant radius plus a small-amplitude random noise,

$$h(\theta,t=0) = [h_0 - \delta \sin(\omega\theta)][1 + \alpha(R_\theta - 0.5)],$$

where $\alpha = 10^{-6}$ and R_θ denotes a random number chosen uniformly between 0 and 1. Results are shown in both Figs. 7(a) and 7(b) with blue dashed lines. As can be seen, the steady state is reached more quickly relative to the case where the perturbation is absent (although not as quickly as in the 2D model). Based on this observation, we conjecture that our GFEM scheme has greater discretization error and this acts like random noise.

In practice, dip coating and spray coating are commonly used to coat the initial film [26–28]. Since an initial film of uniform thickness may be difficult to obtain with these methods, for the rest of this section we only consider the constant-radius initial condition. To show how substrate curvature modifies the liquid distribution, in Figs. 9(b) and 9(c) we plot the steady free-surface profiles obtained from the lubrication model for $\omega = 8$ and $\omega = 5$. With a decrease in pattern frequency, drop size becomes more uniform (note that the number of drops is again equal to ω). The increased uniformity occurs because lower pattern frequency corresponds to larger drop spacing in stage (ii), leading to less interaction (and thus less liquid redistribution) between drops.

Overall, the results from Secs. III A and III B indicate that when the topography amplitude and film thickness are much smaller than the cylinder radius ($\sim$1%), the lubrication model yields predictions that are in quantitative agreement with many of the predictions of the 2D model. Differences arise in predictions of transient behavior and drop location, especially when $S > S_{\text{critical}}$. In addition, the steady free-surface profiles appear to be very sensitive to the initial film condition when $S > S_{\text{critical}}$.

Finally, we briefly summarize the results of some additional calculations we have performed where the topography is nonuniform. If the topography has frequency ω_1 over some portion of the cylinder and ω_2 over the other, then a critical rotation rate can be associated with each of these frequencies. If the rotation rate is below both critical values, drops form over the troughs at steady state. If it is larger than both critical values, drops form over the crests. If the rotation rate is between the critical values, then drops form over troughs on the portion of the surface where the rotation rate is above the corresponding critical value and drops form over the crests on the portion where the rotation rate is below the corresponding critical value. Thus, where the drops are positioned at steady state strongly depends on the local curvature of the surface topography.

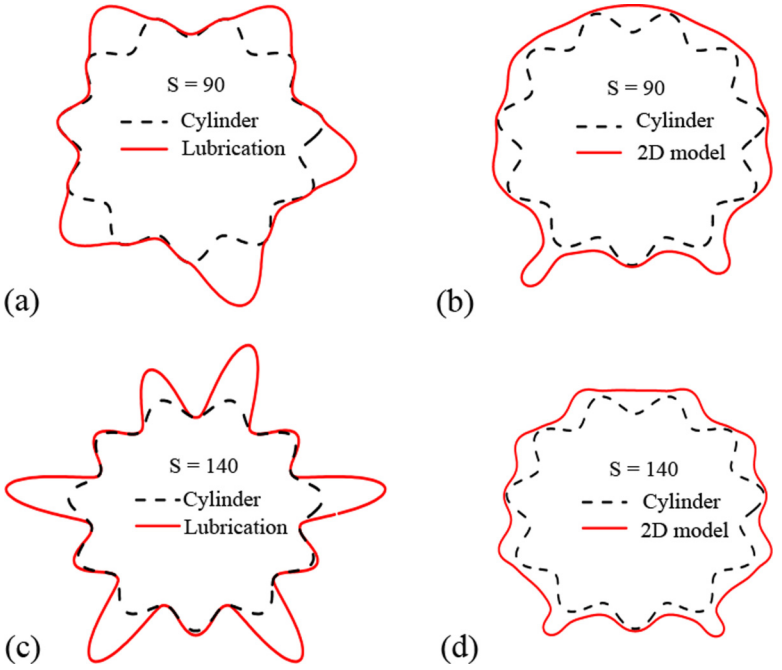

FIG. 10. (a) and (c) Steady free-surface profiles obtained with the lubrication model. (b) and (d) Free-surface profiles just before drop breakoff obtained with the 2D model. In (a) and (b) $S = 90$ and in (c) and (d) $S = 140$. In both cases, $\delta = 0.1$, $\omega = 11$, and $h_0 = 0.13$. Initial conditions are films of constant radius. Dashed lines indicate surface topography.

C. Larger pattern amplitude

To examine the case of larger topography amplitude, we set $\delta = 0.1$, which is now an order of magnitude larger, and perform simulations with both the 2D and lubrication models. Simulations were performed with $h_0 = 0.02$ first, but the film thickness approached zero almost immediately over the crests in both models and could no longer be resolved numerically. To avoid this, we set $h_0 = 0.13$ instead, which is also an order of magnitude larger and comparable to the topography amplitude.

Free-surface profiles for two different values of S are shown in Fig. 10. For $S = 90$, which is less than $S_{\text{critical}} = 120$, the lubrication model predicts that a steady state is attained. As shown in Fig. 10(a), several drops form and are located over pattern troughs, consistent with what was observed in Sec. III A. In contrast, we are unable to find a steady state with the 2D model. Due to the larger film thickness, the drops form more rapidly and highly distorted interface shapes result that are computationally expensive to resolve. For the case shown in Fig. 10(b), two drops located over pattern crests grow rapidly and the simulation must be ended before they break off. We have observed similar behavior for even smaller values of S. (We note that if S becomes too small, the free-surface perturbations grow very slowly and the computation times become prohibitive.)

For $S = 140$, which is greater than $S_{\text{critical}} = 120$, the lubrication model again predicts that a steady state is attained. As shown in Fig. 10(c), this time drops form over the pattern crests, consistent with what was observed in Sec. III B. Again we are unable to find a steady state with the 2D model. For the case shown in Fig. 10(d), drops appear to form over the pattern crests, but two of them grow rapidly and the simulation is once more ended before they break off.

The results of these calculations indicate that for larger pattern amplitudes ($\sim$10% of the cylinder radius), predictions from the lubrication model are not in good agreement with those from the 2D model. As pattern amplitude increases, so does the free-surface curvature as the film thins over the

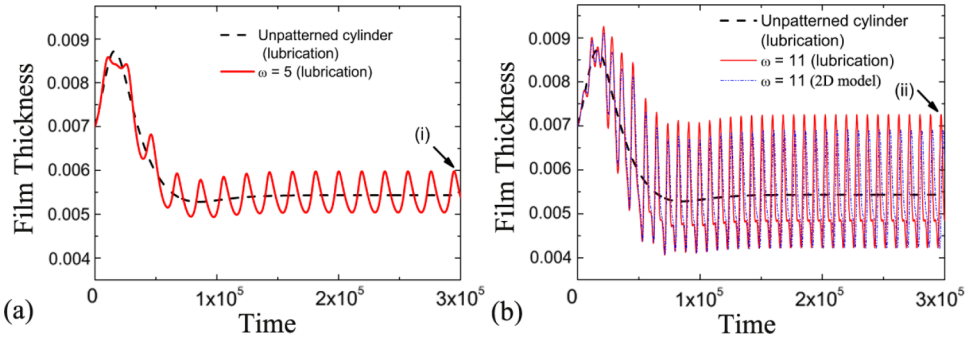

FIG. 11. Time variation of film thickness at $\theta = 3\pi/2$ with $M = 0.1$, Bo $= 100$, $\delta = 0.01$, $h_0 = 0.007$, $W = 0.0007 < W_c$, and (a) $\omega = 5$ and (b) $\omega = 11$. The corresponding film profiles at time (i) and (ii) are shown in Fig. 12.

topography, making the influence of surface tension more pronounced. Since the lubrication model tends to overestimate the effects of surface tension (as noted earlier), it is perhaps not surprising that it more readily predicts steady states when the pattern amplitude is large. Although not shown here, the lubrication model also predicts that free-surface perturbations grow more slowly, consistent with the overestimation of surface tension in that model.

IV. RESULTS FOR GRAVITY EFFECTS

In this section we include the effects of gravity. We first consider small-amplitude topography and then turn to the case of larger-amplitude topography.

A. Small-amplitude topography

To study small-amplitude topography, we set $\delta = 0.01$. Following Ref. [18], all simulations shown here are performed with an initial film of uniform thickness $h_0 = 0.007$. Results of other simulations we have performed indicate that the film profiles at later times are independent of the initial film condition when gravity is significant.

The corresponding critical rotation rate, beyond which a smooth coating can be obtained on an unpatterned cylinder, can be calculated from Moffatt's load condition $W_c = 2.01h_0^2/M$ [3]. For the physical properties listed in Table I, the dimensionless viscosity is $M = 0.1$, and thus $W_c = 0.001$. Results obtained with the 2D model agree well with those from the lubrication model in the parameter regime of this section, so we only show the former in selected cases.

In Fig. 11 we plot the time variation of the film thickness at $\theta = 3\pi/2$ (cylinder bottom) with $W = 0.0007$ ($<W_c$) for $\omega = 0$ (unpatterned cylinder), $\omega = 5$, and $\omega = 11$ at Bo $= 100$. For an unpatterned cylinder with a rotation rate below the critical value, the film thickness reaches a steady state after several revolutions in which a liquid drop forms on the upward-moving side of the cylinder ($3\pi/2 < \theta < 2\pi$) due to gravity-driven drainage [3]. However, when surface topography is present, Fig. 11(a) shows that it triggers a sustained oscillation in film thickness. The coating thus never reaches a true steady state, but rather a quasisteady state. With an increase in pattern frequency, the oscillation becomes more pronounced with higher frequency and amplitude, shown in Fig. 11(b). As can be seen, the results from the 2D model agree well with those from the lubrication model.

To explain why the oscillation becomes more pronounced with increasing ω, we select two time points during the quasisteady stages labeled (i) and (ii) in Figs. 11(a) and 11(b), respectively, and plot the corresponding film-thickness profiles in Fig. 12. The steady thickness profile on an unpatterned cylinder is plotted in the same figure for comparison. For relatively low pattern frequency [Fig. 12(a)], the surface topography barely alters the coating thickness and the film is almost uniform

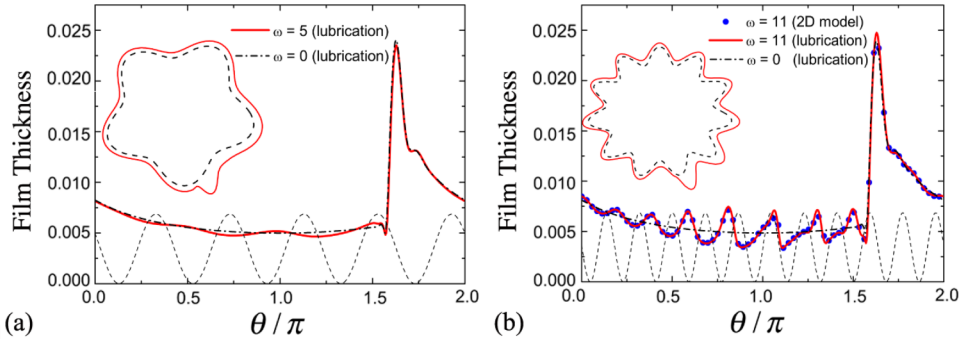

FIG. 12. Film-thickness profiles with $W = 0.0007$ ($<W_c$), $M = 0.1$, Bo $= 100$, $\delta = 0.01$, $h_0 = 0.007$, and (a) $\omega = 5$ at time (i) marked in Fig. 11(a) and (b) $\omega = 11$ at time (ii) marked in Fig. 11(b). Dashed lines indicate surface topography. The insets show the corresponding free-surface profiles. For ease of visualization, the film thickness and pattern amplitude plotted in the insets are ten times larger than the actual values.

within $0 < \theta < 3\pi/2$. This can be attributed to the fact that surface tension only makes a significant contribution to the flow behavior in the region where free-surface curvature is high [3] (i.e., the vicinity of the drop that hangs near the cylinder bottom). As a result, the effects of surface topography dominate the effects of surface tension within $0 < \theta < 3\pi/2$, creating a free-surface shape that has the impression of the topography.

However, an increase in pattern frequency greatly strengthens the effects of surface tension within $0 < \theta < 3\pi/2$, driving liquid from the pattern crests to the pattern troughs. As a consequence, liquid tends to pool more over the troughs, with very thin films forming over the crests [Fig. 12(b)]. This corresponds to a larger variation in film thickness compared to the low-frequency case [Fig. 12(a)] and is consistent with the more pronounced oscillation illustrated in Fig. 11(b). We have also performed simulations with different values of δ and Bo and the results show that either increasing δ or decreasing Bo leads to larger oscillation amplitudes due to stronger surface-tension effects.

For an unpatterned cylinder with rotation rate $W > W_c$, a smooth (Moffatt-type) coating is obtained at steady state, with a thicker film on the upward-moving side and a thinner film on the downward-moving side [1]. Such a coating is desirable for many applications, where the goal is to maintain a nearly uniform film thickness. To facilitate comparison with cases where surface topography is present, we plot the steady film-thickness profiles on an unpatterned cylinder for two different values of Bo in Fig. 13(a). This shows that the steady thickness profile is nearly independent of Bo because surface tension only plays a minor role in the free-surface evolution when $W > W_c$ and surface topography is absent [29,30]. The corresponding free-surface profiles are shown in Fig. 14(a).

For a patterned cylinder with $W > W_c$, the film thickness never reach a true steady state, but it does reach a quasisteady state in which surface topography triggers an oscillation in thickness superimposed on the Moffatt-type coating. We plot in Figs. 13(b) and 13(c) the thickness profiles in the quasisteady state when $M = 100$ and $M = 10$, respectively. When Bo $= 100$, the oscillation in film thickness is much more pronounced on the downward-moving side ($\pi/2 < \theta < 3\pi/2$) than on the upward-moving side. Since the coating is thinner on the downward-moving side, weaker gravitational forces on the liquid on this side are overwhelmed by surface-tension forces, causing more liquid to flow to the troughs on the downward-moving side. This explains the nonuniform oscillation amplitude in film thickness in Fig. 13(b). Again we see that the predictions of the 2D model agree well with those from the lubrication model.

The corresponding free-surface profile for Bo $= 100$ is shown in Fig. 14(b). Here we see that although there are variations in the film thickness, the coating closely conforms to the cylinder surface, a situation that may be desired for many applications. With a decrease in Bo to a value of 10, the variation in film thickness becomes much more uniform [Fig. 13(c)], indicating that

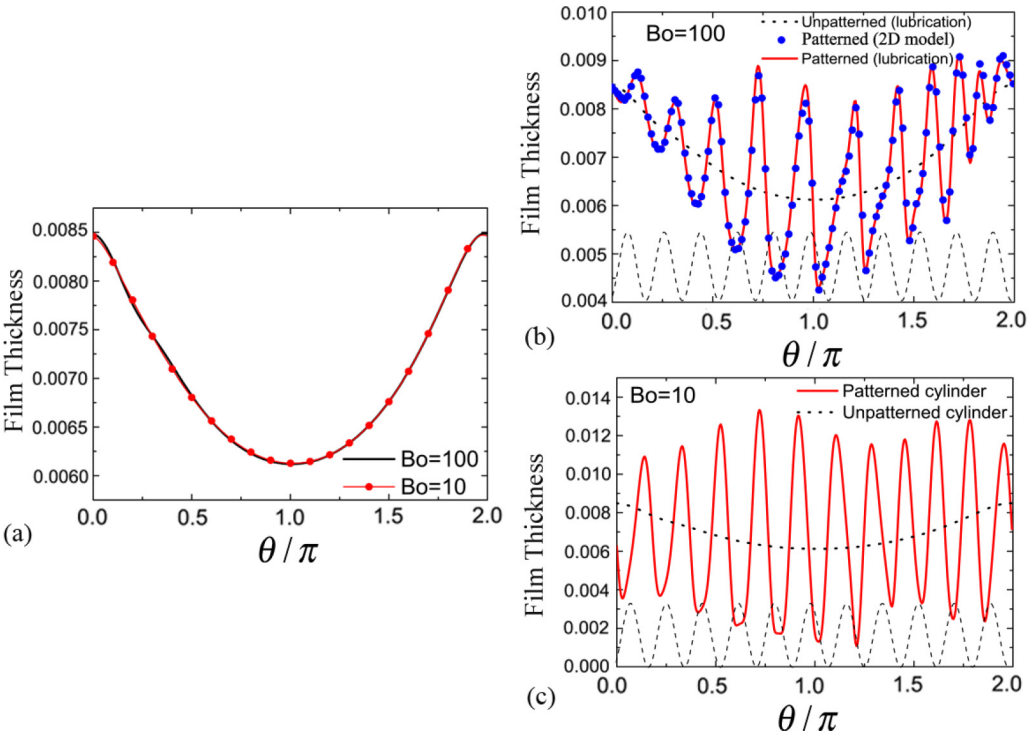

FIG. 13. Film-thickness profiles obtained from the lubrication model at $t = 10^6$ with $W = 0.0012 > W_c$, $M = 0.1$, and $h(\theta,t = 0) = 0.007$: (a) unpatterned cylinder and (b) and (c) patterned cylinder with $\delta = 0.01$ and $\omega = 11$. Results from the 2D model are also shown in (b). Dashed lines at the bottom of (b) and (c) indicate surface topography.

surface-tension forces start to dominate on the upward-moving side as well. The corresponding free-surface profile in Fig. 14(c) shows that the coating does not conform as well to the cylinder surface. Here surface-tension forces are stronger than for Bo $=$ 100 and the resulting capillary flows tend to flatten the coating.

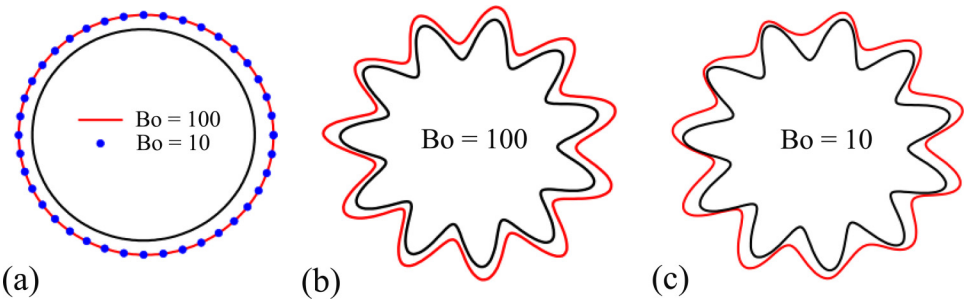

FIG. 14. Free-surface profiles obtained from the lubrication model corresponding to the cases shown in Fig. 13: (a) unpatterned cylinder and (b) and (c) patterned cylinders. For ease of visualization, the film thickness and pattern amplitude plotted are 20 times larger than the actual values.

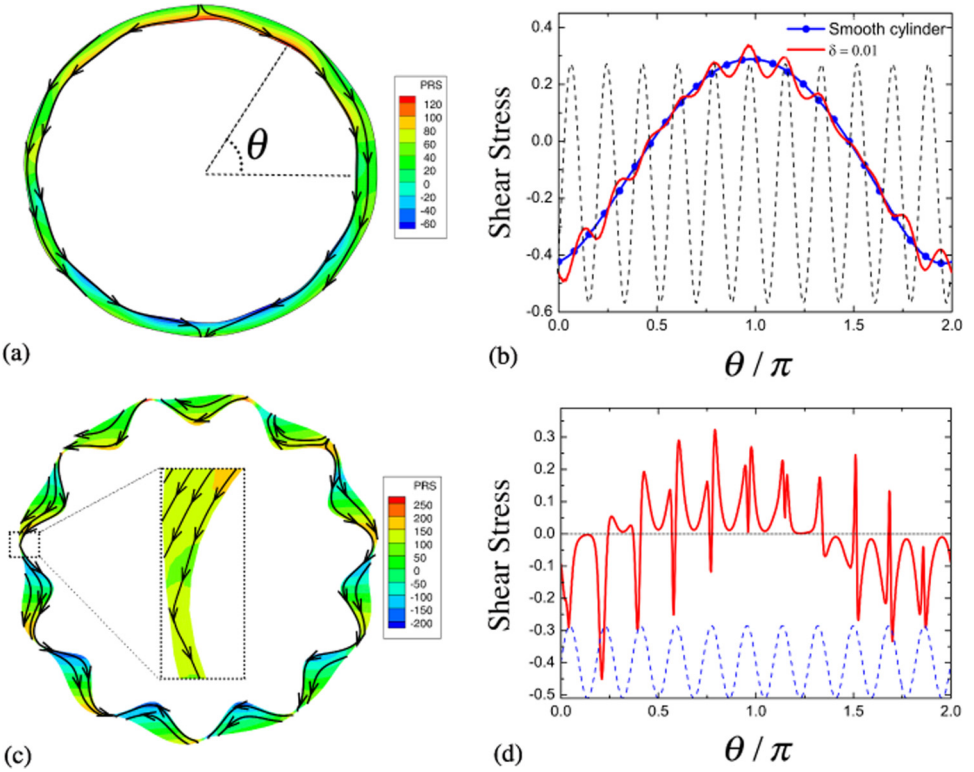

FIG. 15. Streamline patterns, pressure distributions, and shear stress distributions along the cylinder surface with $h_0 = 0.01$, $W = 0.25$, $M = 0.1$, $\omega = 11$, and Bo $= 25$ at $t = 6545$ (25 revolutions) for (a) and (b) $\delta = 0.01$ and (c) and (d) $\delta = 0.1$. Dashed lines indicate surface topography.

B. Larger-amplitude topography

To consider the case where the topography amplitude is larger, we increase δ by an order of magnitude to $\delta = 0.1$. With this amplitude, recirculation regions are observed to form inside the pattern troughs, an important qualitative difference from the small-amplitude case. As noted in the Introduction, the presence of recirculation regions can strongly influence mixing, mass transport, and heat transport. We primarily present results from the 2D model; the validity of the lubrication approximation is discussed toward the end of this section.

As in Sec. III C, a larger initial thickness needs to be used relative to the small-amplitude case to avoid rapid film thinning over the crests that causes the 2D numerical scheme to fail. We choose $h_0 = 0.1$ and again take $M = 0.1$. For these parameters, the critical rotation rate calculated from Moffatt's load condition is $W_c = 2.01 h_0^2$ and $M = 0.201$. We choose a representative value $W = 0.25 > W_c$ to ensure that the thinner film on the downward-moving side of the cylinder will not break. The case $W < W_c$ leads to the formation of a drop on the cylinder (cf. Sec. IV A) and for brevity is not investigated here. We choose a representative value of Bo $= 25$; larger values lead to greater deformation of the free surface (by gravity) that we are not able to resolve computationally.

Figure 15 shows the streamline patterns, pressure distributions, and shear stress distributions along the cylinder surface in the quasisteady state for two different values of δ. The shear stress is calculated from $\tau = \mathbf{n} \cdot \mathbf{T} \cdot \mathbf{t}$, where $\mathbf{T}$ is the total stress tensor. The small-amplitude case ($\delta = 0.01$) presented in this figure serves to facilitate comparison with the larger-amplitude case. Contributions from rigid-body rotation are excluded from the streamline patterns because they do not influence the relative motion of fluid elements or the free-surface shape.

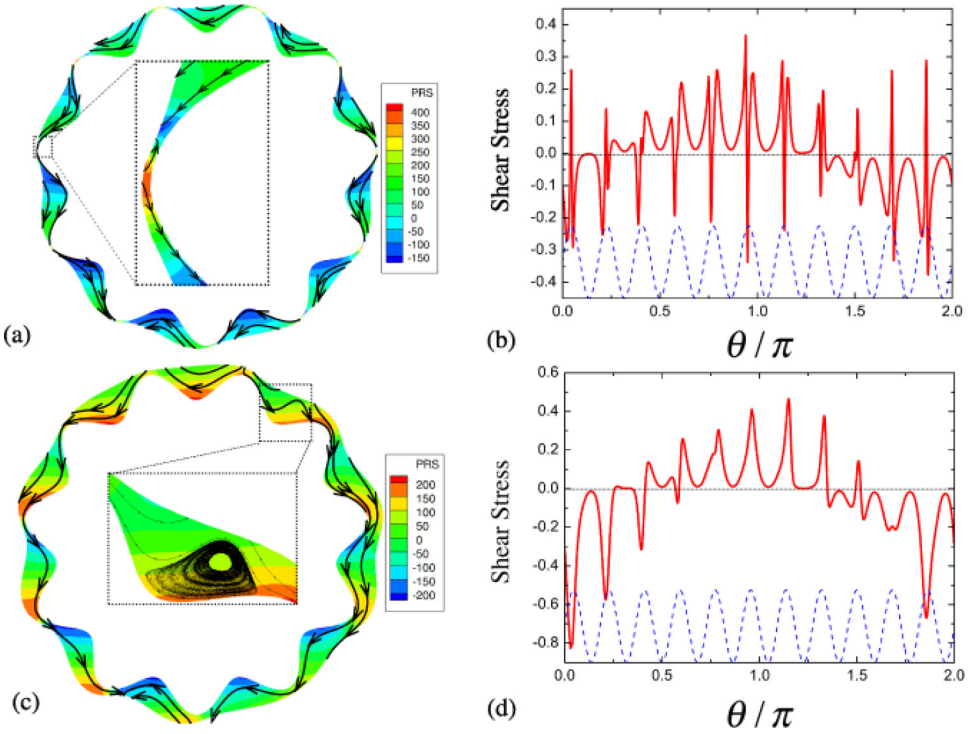

FIG. 16. Streamline patterns, pressure distributions, and shear stress distributions along the cylinder surface with $W = 0.25$, $M = 0.1$, $\omega = 11$, $\delta = 0.1$, and $\mathrm{Bo} = 25$ at $t = 6545$ (25 revolutions) for (a) and (b) $h_0 = 0.08$ and (c) and (d) $h_0 = 0.13$. Dashed lines indicate surface topography.

For the small-amplitude pattern [$\delta = 0.01$, Fig. 15(a)], streamlines originate at the free surface on the upper side of the cylinder and end up at the free surface on the lower side. This corresponds to liquid being driven from the top and sides of the cylinder toward the cylinder bottom by gravitational forces. Near $\theta = \pi$, the corresponding absolute value of the shear stress $|\tau|$ [Fig. 15(b)] decreases over the troughs and increases over the crests. This is due to the deceleration and acceleration of the fluid over the troughs and crests, respectively. Similar behavior was also observed for flows in a wavy channel [31] and over an inclined corrugated wall [11].

For the larger-amplitude pattern [$\delta = 0.1$, Fig. 15(c)], the streamlines originate and terminate at the free surface over each trough. Furthermore, the corresponding shear stress $|\tau|$ [Fig. 15(d)] exhibits local minima over the crests. This is in contrast to the small-amplitude case and reflects rapid deceleration of fluid over the crests. Because the topography has a larger amplitude, the free-surface curvature is greater and this tends to drive liquid into the troughs and hinder the gravity-driven drainage.

Since no flow recirculation is observed for $h_0 = 0.1$, simulations starting with a slightly thinner coating ($h_0 = 0.08$) and a thicker coating ($h_0 = 0.13$) are performed to investigate the influence of film thickness (Fig. 16). When the mean film thickness is smaller than the pattern amplitude [$h_0 = 0.08$, Fig. 16(a)], reverse flows form over the crests and their direction is opposite to that of the gravity-driven drainage flow, preventing escape of liquid from the troughs. As a consequence, liquid that initially accumulates inside a given trough will be kept there as the cylinder rotates. The enlargement of the boxed region in Fig. 16(a) demonstrates that these reverse flows can be attributed to the buildup of capillary pressure over the crests. As shown in Fig. 16(b), the corresponding shear stress in the high-pressure regions (i.e., pattern crests) changes sign over the crests, indicating the acceleration of the liquid in the direction opposite to that of the gravity-driven drainage.

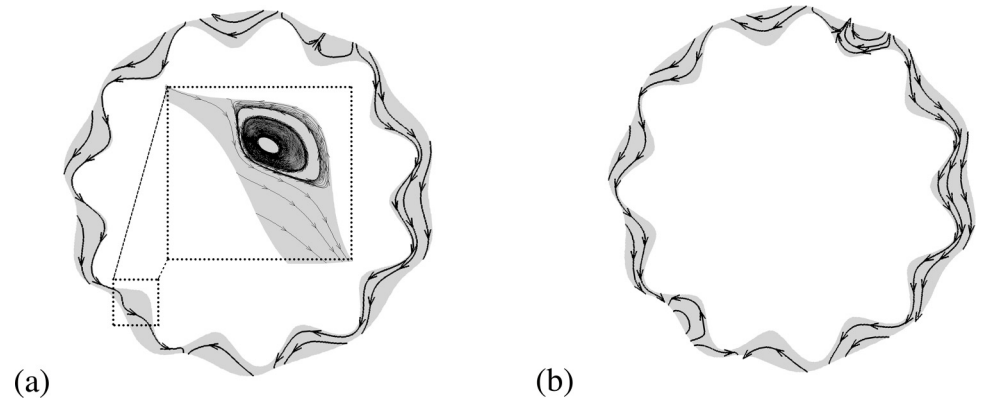

FIG. 17. Streamline patterns with $W = 0.25$, $M = 0.1$, $\omega = 11$, $\delta = 0.1$, Bo $= 25$, and $h_0 = 0.13$ at (a) $t = 6548$ and (b) $t = 6551$.

When the mean film thickness is larger than the pattern amplitude [$h_0 = 0.13$, Fig. 16(c)], gravitational forces become more significant, which suppresses the flow reversal over the crests. However, a recirculation region now forms inside the trough on the upward-moving side of the cylinder, which may influence the mixing, mass transport, and heat transport in that region [11,15–17]. A detailed study of this issue would be valuable but is beyond the scope of the present paper.

To further characterize the recirculation regions, we plot in Fig. 17 the streamline patterns at slightly later times. Note that the three points in time selected in Figs. 16(c), 17(a), and 17(b) are all within $1/\omega$ of a complete revolution. As the cylinder rotates, the first recirculation region vanishes, while a second one forms on the downward-moving side, as shown in Fig. 17(a). Both recirculation regions vanish at a later stage [Fig. 17(b)] and will not form again until the coating is restored to the condition shown in Fig. 16(c).

These phenomena can be understood by considering the variation in the pattern inclination angle. For film flow along an inclined wall with topography, it is known that recirculation regions form inside the troughs only when the film thickness is larger than some critical value. This critical value is highly sensitive to the substrate inclination angle [11,12,14]. For a patterned cylinder, the inclination angle of each trough varies constantly as the cylinder rotates, leading to an oscillation in the critical film thickness and thus formation and vanishing of recirculation regions over time.

To investigate the extent to which the lubrication model is still applicable, we show in Fig. 18 the free-surface profiles calculated with both the 2D model and the lubrication model for $\delta = 0.1$, $\omega = 11$, and $h_0 = 0.13$. The profiles show better agreement on the downward-moving side, where surface-tension forces overwhelm gravitational forces due to the smaller film thickness. The same parameter combination of h_0, δ, and ω is considered in the regime where centrifugal forces dominate (Fig. 10) and the lubrication model fails to describe the steady free-surface shape. Noting that $S = \rho\Omega^2 R_{\text{mean}}^3/\sigma = W^2\text{Bo}$, we find that $S \sim 1$ for the calculations in Fig. 18, meaning that surface-tension forces are comparable to centrifugal forces. In contrast, $S = 90$ in Fig. 10 and centrifugal forces dominate. We therefore infer that strengthening surface tension flattens the free surface and, as a result, the validity of the lubrication model improves.

Finally, we briefly summarize the results of some additional runs we have performed in which the topographical pattern has a trapezoidal-like shape. The trapezoidal-like patterns are steeper than the sinusoidal patterns and are relevant to applications such as 3D printing (Fig. 1) mentioned in the Introduction. Similar patterns have also been used to study thin-film flows on planar substrates [7,10,32,33]. Similar to the planar case, we find that the film can form capillary ridges over the topography mounds and that minima in the film thickness can develop near the mound corners. The sizes of the ridges and minima are nonuniform due to the nonuniformity of gravitational forces around the cylinder. Both the ridges and minima are usually undesired since the former create coating

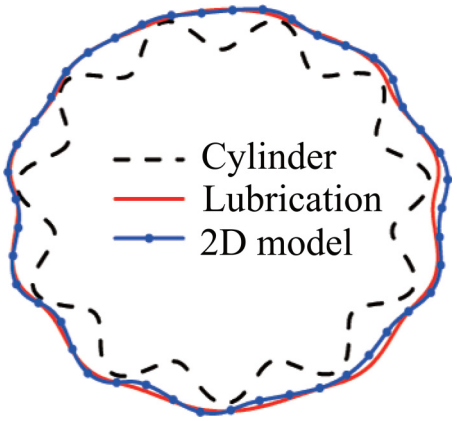

FIG. 18. Free-surface profiles with $W = 0.25$, $M = 0.1$, $\omega = 11$, $\delta = 0.1$, Bo $= 25$, and $h_0 = 0.13$ at $t = 6545$ (25 revolutions).

nonuniformity and the latter are especially susceptible to film rupture. As with the planar case, these features become more pronounced as the topographical features become steeper, and the lubrication model does not predict well the detailed free-surface shape near the pattern corners.

V. CONCLUSIONS

The results of this work demonstrate that even small-amplitude surface topography ($\sim$1% of the cylinder radius) can have a significant influence on thin-film flows on rotating cylinders. Results from a full 2D model agree well with those from a model based on lubrication theory provided the free-surface curvatures are sufficiently small, an outcome that represents a significant benchmark for the lubrication model. In general, the free-surface curvatures become larger as the topography amplitude increases and, as a result, the accuracy of the lubrication model worsens.

For many practical applications, it is of interest to consider three-dimensional effects that arise due to surface topography or to Rayleigh-Taylor-like or Rayleigh-Plateau-like instabilities (see, e.g., Ref. [34]). The lubrication model can readily be extended to three dimensions [4], and because 3D calculations are much less computationally expensive with the lubrication model, it provides an efficient vehicle for studying axial variations.

For certain applications, it may be desirable to use a coating to planarize a substrate. In other applications, a coating that conforms to the substrate topography is desired. Our results indicate that if gravitational forces become significant, then it should be possible to obtain a coating that closely conforms to the substrate topography due to the interplay between gravity, surface tension, and rotation (Sec. IV). Rotating the cylinder too quickly will initiate instabilities that result from a competition between surface tension and centrifugal forces and interact in a complicated way with the surface topography (Sec. III). Planarization would likely require a relatively thick initial coating followed by simultaneous rotation and drying to counteract the effects of gravitational drainage. Drying may initiate Marangoni flows [35,36] due to temperature or composition effects, but the lubrication model can readily be extended to account for these effects.

ACKNOWLEDGMENT

This work was supported through the Industrial Partnership for Research in Interfacial and Materials Engineering of the University of Minnesota. We are grateful to the Minnesota Supercomputing Institute (MSI) at the University of Minnesota for providing computational resources.

[1] H. K. Moffatt, Behaviour of a viscous film on the outer surface of a rotating cylinder, J. de Mécanique **16**, 651 (1977).
[2] V. V. Pukhnachev, Motion of a liquid film on the surface of a rotating cylinder in a gravitational field, J. Appl. Mech. Tech. Phys. **18**, 344 (1977).
[3] P. L. Evans, L. W. Schwartz, and R. V. Roy, Steady and unsteady solutions for coating flow on a rotating horizontal cylinder: Two-dimensional theoretical and numerical modeling, Phys. Fluids **16**, 2742 (2004).
[4] P. L. Evans, L. W. Schwartz, and R. V. Roy, Three-dimensional solutions for coating flow on a rotating horizontal cylinder: Theory and experiment, Phys. Fluids **17**, 072102 (2005).
[5] S. K. Wilson, R. Hunt, and B. R. Duffy, On the critical solutions in coating and rimming flow on a uniformly rotating horizontal cylinder, Q. J. Mech. Appl. Math. **55**, 357 (2002).
[6] R. C. Peterson, P. K. Jimack, and M. A. Kelmanson, On the stability of viscous free-surface flow supported by a rotating cylinder, Proc. R. Soc. London A **457**, 1427 (2001).
[7] L. E. Stillwagon and R. G. Larson, Fundamentals of topographic substrate leveling, J. Appl. Phys. **63**, 5251 (1988).
[8] D. Perizzolo, W. R. Lacefield, and D. M. Brunette, Interaction between topography and coating in the formation of bone nodules in culture for hydroxyapatite- and titanium-coated micromachined surfaces, J. Biomed. Mater. Res. **56**, 494 (2001).
[9] J. Zhu, J. L. Chen, R. K. Lade, Jr., W. J. Suszynski, and L. F. Francis, Water-based coatings for 3D printed parts, J. Coatings Technol. Res. **12**, 889 (2015).
[10] R. V. Craster and O. K. Matar, Dynamics and stability of thin liquid films, Rev. Mod. Phys. **81**, 1131 (2009).
[11] C. Pozrikidis, The flow of a liquid film along a periodic wall, J. Fluid Mech. **188**, 275 (1988).
[12] A. Wierschem, M. Scholle, and N. Aksel, Vortices in film flow over strongly undulated bottom profiles at low Reynolds numbers, Phys. Fluids **15**, 426 (2003).
[13] M. Scholle, A. Wierschem, and N. Aksel, Creeping films with vortices over strongly undulated bottoms, Acta Mech. **168**, 167 (2004).
[14] M. Scholle, A. Haas, N. Aksel, M. C. T. Wilson, H. M. Thompson, and P. H. Gaskell, Competing geometric and inertial effects on local flow structure in thick gravity-driven fluid films, Phys. Fluids **20**, 123101 (2008).
[15] A. Wierschem and N. Aksel, Influence of inertia on eddies created in films creeping over strongly undulated substrates, Phys. Fluids **16**, 4566 (2004).
[16] M. Scholle, A. Haas, N. Aksel, H. M. Thompson, R. W. Hewson, and P. H. Gaskell, The effect of locally induced flow structure on global heat transfer for plane laminar shear flow, Int. J. Heat Fluid Flow **30**, 175 (2009).
[17] J. Nam, L. E. Scriven, and M. S. Carvalho, Tracking birth of vortex in flows, J. Comput. Phys. **228**, 4549 (2009).
[18] A. K. Sahu and S. Kumar, Thin-liquid-film flow on a topographically patterned rotating cylinder, Phys. Fluids **26**, 042102 (2014).
[19] G. K. Batchelor, *An Introduction to Fluid Dynamics* (Cambridge University Press, Cambridge, 1967).
[20] M. A. Kelmanson, On inertial effects in the Moffatt-Pukhnachov coating-flow problem, J. Fluid Mech. **633**, 327 (2009).
[21] K. N. Christodoulou, S. F. Kistler, and P. R. Schunk, in *Liquid Film Coating*, edited by S. F. Kistler and P. M. Schweizer (Chapman & Hall, London, 1997), pp. 297–397.
[22] M. Luskin, R. Rannacher, and W. Wendland, On the smoothing property of the Crank-Nicolson scheme, Appl. Anal. **14**, 117 (1982).
[23] S. Dodds, M. da Silveira Carvalho, and S. Kumar, Stretching and slipping of liquid bridges near plates and cavities, Phys. Fluids **21**, 092103 (2009).
[24] See Supplemental Material at http://link.aps.org/supplemental/10.1103/PhysRevFluids.2.024001 for a derivation.
[25] P. L. Evans, Mathematical and numerical investigations of coating flows, Ph.D. thesis, University of Delaware, 2000.

[26] W. L. Mckown and P. K. Zietlow, Process for sugar coating ready-to-eat cereal, US Patent No. 3615676 (26 October 1971).
[27] T. Yamamoto, T. Takeo, K. Ichinose, S. Ozawa, K. Fujii, M. Enomoto, I. Ishibashi, and J. Murayama, Method for uniformly painting an object with moving spray guns spaced a constant distance from the surface of the object, US Patent No. 5240745 (31 August 1993).
[28] J. Biteau, C. Ford, and A. Glacet, Method of dip-coating a lens, US Patent No. 20130022739 (24 January 2013).
[29] E. B. Hansen and M. A. Kelmanson, Steady, viscous, free-surface flow on a rotating cylinder, J. Fluid Mech. **272**, 91 (1994).
[30] E. J. Hinch and M. A. Kelmanson, On the decay and drift of free-surface perturbations in viscous thin-film flow exterior to a rotating cylinder, Proc. R. Soc. London A **459**, 1193 (2003).
[31] C. Pozrikidis, Creeping flow in two-dimensional channels, J. Fluid Mech. **180**, 495 (1987).
[32] S. Kalliadasis, C. Bielarz, and G. M. Homsy, Steady free-surface thin film flows over topography, Phys. Fluids **12**, 1889 (2000).
[33] S. Kalliadasis and G. M. Homsy, Stability of free-surface thin-film flows over topography, J. Fluid Mech. **448**, 387 (2001).
[34] J. R. Lister, J. M. Rallison, A. A. King, L. J. Cummings, and O. E. Jensen, Capillary drainage of an annular film: The dynamics of collars and lobes, J. Fluid Mech. **552**, 311 (2006).
[35] C. Pozrikidis, Effect of surfactants on film flow down a periodic wall, J. Fluid Mech. **496**, 105 (2003).
[36] W. Li and S. Kumar, Thin-film coating of surfactant-laden liquids on rotating cylinders, Phys. Fluids **27**, 072106 (2015).